ChemComm

Highly Conductive, Transparent Molecular Charge-Transfer Salt with Reversible Lithiation

SCHOLARONE™
Manuscripts

COMMUNICATION

Highly Conductive, Transparent Molecular Charge-Transfer Salt with Reversible Lithiation

Ying-Shi Guan[a,b], Yong Hu[a,b], Hanguang Zhang[c], Gang Wu,[c]* Hao Yan,[d]* Shenqiang Ren[a,b]*

Here we describe the high conductivity in molecular charge-transfer hydrocarbon both as bulk solid and films. Specially, the high electrical conductivity (~ 30 S/cm) and transparency (~80%) of TTF-TCNQ thin films allow us develop its application in all-organic freestanding photodetectors. More importantly, the fabricated TTF-TCNQ thin film can be used in lithium-ion battery electrode with a specific capacity of ~250 mAh/g.

Metallic conduction in conjugated polymers has been extensively studied in poly(3,4-ethylenedioxythiophene, (PEDOT)) doped with poly(4-styrenesulfonate, (PSS)), polyaniline, and polypyrrole.[1-3] Although numerous potential applications are emerging, the tremendous influences of molecular packing and intentional doping are still a matter of discussion. Up to now, it is still a challenge to synthesize high-performance metallic polymer due to its complex synthetic procedures with low yields. Secondly, achieving high conductivity is confined to chemical doping which can reversely affect the stability of polymer materials. Thirdly, macromolecular backbone structure of conjugated polymers usually provides the poor transparency at the visible range.[4] To address these challenges, molecular metals have been reported in certain charge-transfer (CT) salts,[5-7] in which the counter ions can stabilize charge carriers and strong molecular interaction can be generated simultaneously.

Metallic conduction in molecular aromatic hydrocarbon materials, as a new class of electronic solids, requires strong intermolecular orbital interaction between molecules and high carrier density.[8,9] It was found that the metallic conductivity of molecular salts is associated with its crystal structures, π-electron overlap, and charge-transfer interactions.[10] Depending on the nature of the interaction between the electrons, a quasi-one-dimensional system may exist in different electronic states.[11] Extensive efforts have been devoted to studying

molecular metal tetrathiafulvalene–tetracyanoquinodimethane (TTF-TCNQ), in which the electrons in the highest occupied molecular orbital (HOMO) of TTF donor molecule are transferred to the lowest unoccupied molecular orbital (LUMO) of TCNQ acceptor.[12-15] As a result, the TTF and TCNQ chains behave as a quasi-one-dimensional electronic system which shows metallic conductance along the π-overlap stack (b-axis), in a wide temperature range from room temperature down to 54 K where a Peierls transition is observed. While the low work function of TTF-TCNQ makes it suitable as a contact material, a strongly anisotropic electrical conductivity along the a- and b-axis of pseudo-one-dimensional TTF-TCNQ metal makes it challenging for the use of electronics.[16-22] Here, we report high conductivity in molecular TTF-TCNQ solid, in which the pressure-dependent packing structure is studied with regard to the electronic conductivity. A high electrical conductivity (~ 30 S/cm) and transparency (~80%) of TTF-TCNQ thin films, as well as its low contact resistance with conjugated polymers, enable the development of all-organic freestanding photodetectors with a low bias voltage, suggesting its application potential for transparent molecular electronics. The transparent TTF-TCNQ electrode further enables reversible Li storage, as a new type of anode materials for lithium-ion battery with a specific capacity of ~250 mAh/g.

The choice of TTF donor and TCNQ acceptor molecules is motivated by the synthesis of organic metallic crystal (Figure 1a), where its low contact resistance at the organic interface is indispensable to enable organic electronics. The TTF-TCNQ crystal comprises of uniformly segregated and parallel stacks of TTF and TCNQ with the π-π molecular orbitals being primarily overlapped along the stacking direction, leading to its 1D metallic transport behavior. The overlap of π orbitals along the stack direction causes a giant anisotropic conductivity. This unique molecular stacking structure enables the TTF-TCNQ with a record room-temperature high conductivity in molecular materials. The as-grown TTF-TCNQ single crystals are then ground and pressed to prepare the solid pellet with a diameter of 10 mm. The structural morphology and chemical composition mapping of the pellet is investigated using scanning electron microscopy (SEM) and energy-dispersive X-ray spectroscopy (EDS, Figure 1b), which suggests the uniform distribution of TTF-

a. Department of Mechanical and Aerospace Engineering, University at Buffalo, The State University of New York, Buffalo, NY 14260, USA. shenren@buffalo.edu
b. Research and Education in eNergy, Environment and Water (RENEW) Institute, University at Buffalo, The State University of New York, Buffalo, NY 14260, USA.
c. Department of Chemical and Biological Engineering, University at Buffalo, The State University of New York, Buffalo, NY 14260, USA. gangwu@buffalo.edu
d. Center for High Pressure Science and Technology Advanced Research, Shanghai, 201203, P.R. China. yanhao@hpstar.ac.cn

TCNQ cocrystal. The characteristic principal vibration modes at 1202 cm^{-1} (C=CH bending), 1412 cm^{-1}(C-CN wing stretching), 1603 cm^{-1} (C=C ring stretching), and 2208 cm^{-1} (CN stretching) confirm that the presence of TTF and TCNQ phases in the pellet (Figure 1c).[23] In-situ temperature-dependent synchrotron X-ray powder diffraction suggests its stability of TTF-TCNQ crystal pellet from 298 K to 438 K (Figure 1d), while the molecular ordering gradually decreases as the temperature is raised further.
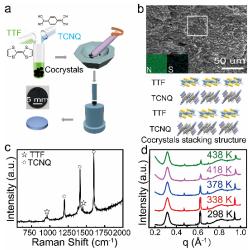

Figure 1. (a) The schematic diagram for the fabrication of TTF-TCNQ bulk samples. (b) The SEM image of the TTF-TCNQ pellet and the stacking structure of the TTF-TCNQ cocrystals. (c) The raman spectrum of TTF-TCNQ crsytals. (d) The XRD data of TTF-TCNQ crystal under different temperaure.

In addition, pressure, as one of the thermodynamic variables, can drastically alter the lattice and electronic configuration of TTF-TCNQ crystals. As shown in Figure 2a, we apply the synchrotron X-ray diffractometry to monitor the crystal structure of TTF-TCNQ under different pressures through uniaxial compression, suggesting the pressure effect on the enhancement of molecular ordering and electronic density.[24] The resistances of the pellets under different pressure are performed in a ^{4}He cryostat with the temperature range from 300 K to 4.2 K (Figure 2b). The pressure dependence influences the interaction of the electronic wave functions between TTF and TCNQ, which can increase the overlap of the π-π molecular orbitals to alleviate the quasi-one-dimensional conductivity of TTF-TCNQ.[16,25] The conductivity increases as raising the uniaxial compression which provides a powerful tool to study the dominant microscopic interaction, that drives the anisotropic overlapping integrals between the adjacent molecules. In addition, the pressure induced modulation of the charge transfer ratio between TTF and TCNQ can lead to the commensurability of charge density wave due to the molecular structure packing.[26,27] In addition, the resistivity of the solid does not show the temperature-dependent or thermal stress induced hysteretic behavior. All samples show a consistent Peierls transition at ~54 K (Figure S1), where the resistivity increases sharply. The measurement of temperature-dependent resistivity of TTF-TCNQ pellets are of particular interest, while it is essential to employ the four-terminal configuration (Figure 2c-2d). The resistivity of TTF-TCNQ pellets ranges from 5.5 x 10^{-3} Ω cm to 4.5 x 10^{-2} Ω cm with decreasing

the temperature from 300 K to 100 K, respectively. The resistivity of TTF-TCNQ solids is observed to gradually increase with decreasing the temperature, suggesting that the charge transport is dominant by thermally activated hopping.
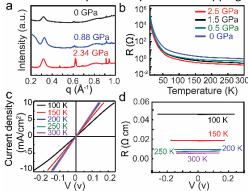

Figure 2. (a) The XRD data of TTF-TCNQ crystal under different pressure. (b) The temperature-dependent resistance of the TTF-TCNQ bulk samples under different pressure. (c) The I-V curves of the TTF-TCNQ bulk samples at different temperature. (d) The R-V curves of the TTF-TCNQ bulk sample at different temperature.

The lack of flexibility in these molecular crystal powders made it challenging to determine its electronic performance in all-organic electronics. The thin film morphology of TTF-TCNQ crystals could demonstrate unique highly conductive feature, optical transparency and low contact resistance with conjugated polymers. Therefore, we evaluate how the charge-transfer nature of transparent TTF-TCNQ thin films can affect its transport behaviors. The growing thickness of thin films from 100 nm to 1000 nm, through the evaporation of TTF-TCNQ single crystals, consist of highly oriented and strongly textured microcrystals composing of high-aspect-ratio nanowires (Figure 3a-3b and S2-S3). The XRD pattern for a typical TTF–TCNQ thin film exhibits (00l) reflection, indicating the (002) molecular planes (ab-planes) of the films aligned parallel to the substrate surface (Figure S4). The TTF-TCNQ films with different thickness have a similar preferential growth orientation revealed by the XRD, although the morphology of the thin films with different thickness are different due to the different evaporation temperature during the growth process. Figure 3c presents the transmittance spectra of TTF–TCNQ thin films, on which the transmittance is decreased from 93% to 36% at 550 nm wavelength with increasing the film thickness from 100 nm to 1000 nm. The thickness dependent electrical conductivity of the TTF–TCNQ films is shown in Figure 3d. The conductivity is observed to gradually increase with increasing the thickness below 200 nm, while the transmittance is observed to decrease with increasing the thickness. The optimum TTF–TCNQ thin films has a conductivity of 30 S/cm and transmittance of ~80% at 550 nm wavelength. The relationship between transmittance and sheet resistance of TTF-TCNQ can be characterized by the figure of merit (FOM), which is defined as the ratio of direct current conductivity (σ_{dc}) to optical conductivity (σ_{op}).[28-29]

$$\text{FOM} = \frac{\sigma_{dc}}{\sigma_{op}} = \frac{188.5\,\Omega}{R_{sheet}(T^{\left(-\frac{1}{2}\right)}-1)} \quad (1)$$

where R$_{sheet}$ is the sheet resistance and T is the transmittance at 550 nm. When compared with other materials used for transparent electrode, the performance of TTF-TCNQ is about

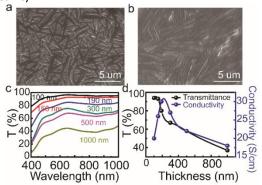equivalent to other materials with high transparency and high conductivity.

Figure 3. (a-b) The SEM images of the TTF-TCNQ film with different thickness (100 nm for a and 300 nm for b). (c) The transmittance of the TTF-TCNQ film with different thickness (from 100 nm to 1000 nm). (d) The thickness dependent transmittance at 550 nm and the thickness dependent conductivities of the TTF-TCNQ film.

For the highly conductive TTF-TCNQ thin films with the optimum electric conductivity and transmittance, its temperature dependent resistivity is studied in the range between 20 K and 298 K based on the four-terminal configuration (Figure 4a). The resistivity is observed to gradually decrease with the increase of the temperature, suggesting that the charge transport is dominant by thermally activated hopping probability within the TTF-TCNQ films. It should be noted that the Peierls transition (54 K) of TTF-TCNQ films does not change over TTF-TCNQ bulk crystals (Figure S5). The temperature dependent transport behaviors of TTF-TCNQ films are studied in the range between 100 K and 298 K through the current-voltage (I-V) and resistivity-voltage (R-V) measurements (Figure 4b-4c). The resistivity of the TTF-TCNQ film decrease from 2900 Ω cm to 0.033 Ω cm with the temperature increasing from 100 K to 298 K. The conductivity of the bulk TTF-TCNQ is higher than that of the TTF-TCNQ thin films, which is mainly due to the existing grain boundaries in the film samples.
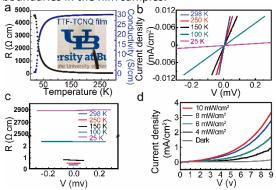

Figure 4. (a) The temperature-dependent resistivity and conductivity of the TTF-TCNQ film with optimum transparency and conductivity. Inset: the photograph of the TTF-TCNQ film. (b) The I-V curves of the TTF-TCNQ film with optimum transparency and conductivity at different temperature. (c) The R-V curves of the TTF-TCNQ film with optimum transparency and conductivity at different temperature. (d) The current density-voltage curves of the all-organic photodetector under light illumination with different intensities.

Highly conductive and transparent TTF-TCNQ thin films show the great potential for the development of all-organic freestanding electronics.[28] We fabricate the flexible photodetectors consisting of the freestanding organic conjugated polymer poly(3-butylthiophene-2,5-diyl)-C_{60} charge

transfer complex (Pth-C_{60}) nanosheet and transparent TTF-TCNQ electrode (Figure 4d). The current-voltage (I-V) characteristics measured in the dark and under illumination with a white light source at different power intensities are shown in Figure 4d. The maximum responsivity of the photodetector (334 mA/W) can be calculated using the following equation: $R = I_{ph} /PS$, where I_{ph} is the photocurrent, P is the incident light intensity, and S is the effective area of the device. The on-off photoresponse cycles of the flexible photodetector are shown in Figure S6, which exhibits high current on/off ratio of ~21, and high response speed (300 ms). As a comparison, the control photodetector is shown using the freestanding conjugated polymer Pth-C_{60} nanosheet and ITO electrode (Figure S7), the maximum responsivity of which is about 293 mA/W. The results reveal that the performance of the devices with TTF-TCNQ thin film electrode are comparable even better than that of the devices with ITO electrode.
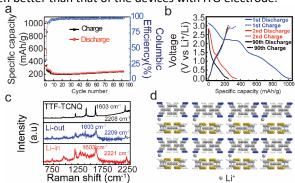

Figure 5. (a) Cycle performance of lithium-ion battery using TTF-TCNQ as the anode. (b) The discharging/charging curves of the lithium-ion battery using TTF-TCNQ as the anode. (c) The Raman spectra of the TTF-TCNQ film at different stages of Li intercalation. (d) The schematic diagram of the Li ion storage.

The profound high conductivity of molecular TTF-TCNQ films show its promising lithium storage capability, as a binder-free and carbon conductor-free electrode in lithium-ion battery. The TTF-TCNQ anode is observed to store lithium-ions reversibly at the voltage window between 0.005 V and 3.0 V at a current density of 20 mA/g for 92 cycles (Figure 5a). The first cycle of discharge has a capacity of 1026 mAh/g, while the discharge capacity diminishes to 348 mAh/g in the second cycle and becomes stable at 220 mAh/g after 9 cycles (Figure 5a). The decrease in capacity for first several cycles is attributed by the formation of solid electrolyte interphase (SEI), resulting in part of irreversible lithiation at low potential. After 90th cycles, the discharge specific capacity still retained 250 mAh/g, even higher than the capacity at the 9th cycle (220mAh/g), which may contribute to the expanded layer structure of TTF-TCNQ to store more lithium-ions. When compared with other organic anode materials in lithium-ion batteries, TTF-TCNQ is one of the state-of-art anode for lithium-ion batteries in terms of small organic moelecules (Table S1). The voltage-discharge/charge profile reveals the lithium-ions interacting with TTF-TCNQ (Figure 5b). Flat plateaus in first discharge appear at 2.2 V, suggesting the redox reactions with lithium-ions probably taking place on redox function groups instead of phenyl rings.[30] On the other hand, the voltage-discharge profiles in 2nd and 90th presented no plateaus, implying the possible lithiation in the layer

COMMUNICATION

structure among phenyl rings.[31] Such behavior was also confirmed by the cyclic voltammetry of TTF-TCNQ electrode in the coin cell (Figure S8). The peak at 0.5 V during the discharge disappeared after second cycle implying the formation of SEI in the first cycle. Besides, no peak above 2 V was observed in the discharge after the 3rd cycle, which suggests that no redox reaction on the TTF-TCNQ electrode at voltage above 2 V. This is in agreement with the observation in the discharge-charge profiles that the capacity of TTF-TCNQ comes from the interculation of Li-ions between its layer structure. To further confirm the redox reactions position of the TTF-TCNQ-Li interaction, Raman spectroscopy has been used to identify the vibrational modes resulting from different chemical bonds between Li atoms and TTF-TCNQ complexes. The Raman spectra at different stages of TTF-TCNQ-Li intercalation are shown in Figure 5c. The characteristic principal vibration mode at 1603 cm^{-1} (C=C ring stretching), 1202 cm^{-1} (C=CH bending) exhibits no obvious shift, while the vibration mode at 2208 cm^{-1} (C-CN stretching) changes upward to 2221 cm^{-1} at the charge stage and backward to 2209 cm^{-1} at the discharge stage, especially, new vibration mode at 1337 cm^{-1} (C-CN wing stretching) at charge stage (Li in state) which can be attributed to the charge transfer interactions between atomic Li and TCNQ. This result indicates that the Li-ions mainly intercalate into the TTF-TCNQ layer through interacting with TCNQ, depicted in Figure 5d. The realization of quasi-one-dimensional TTF-TCNQ conductor with highly conductive charge-transfer channel offers an unprecedented versatility for the lithium-ion transport, which has the potential to assemble lithium-ion batteries.

Given the similarity of highly conductive TTF-TCNQ solids to other charge-transfer complexes, similar consideration of highly conductive transparency and reversible Li storage capability may also hold true for the molecular layered crystals with high charge carrier density. The virtually infinite classes of molecular stacked conductors can provide an unprecedented versatility to tune electronic properties. The high electrical conductivity of the TTF-TCNQ film with simultaneously high transparency enable the development of all-organic freestanding photodetectors serving as transparent electrode. Overall, the temperature-dependent conductance of TTF-TCNQ crystals suggests its charge transport dominant by thermally activated hopping. Furthermore, our results show that highly conductive and transparency of TTF-TCNQ thin films have great potential for the development of all-organic transparent freestanding electronics and anode materials in lithium-ion batteries.

Conflicts of interest

There are no conflicts to declare.

Funding Sources

Notes and references

1   I. Y. Choi, J. Lee, H. Ahn, J. Lee, H. C. Choi, M. J. Park, Angew. Chem., Int. Ed. 2015, 54, 10497-10501.
2   B. J. Worfolk, S. C. Andrews, S. Park, J. Reinspach, N. Liu, M. F. Toney, S. C. B. Mannsfeld, Z. Bao, Proc. Natl. Acad. Sci. 2015, 112, 14138-14143.
3   D. D. Ateh, H. A. Navsaria, P. Vadgama, J. R. Soc. Interface 2006, 3, 741-752.
4   Y. Joo, V. Agarkar, S. H. Sung, B. M. Savoie, B. W. Boudouris, Science 2018, 359, 1391-1395.
5   Y. Hu, G. Zhong, Y.-S. Guan, N. H. Lee, Y. Zhang, Y. Li, T. Mitchell, J. N. Armstrong, J. Benedict, S.-W. Hla and S. Ren, Adv. Mater., 2019, 31, 1807178.
6   Y. Hu, G. Zhong, Y.-S. Guan, J. N. Armstrong, C. Li, C. Liu, A. N'Diaye, A. Bhattacharya and S. Ren, Small, 2019, 15, 1900299.
7   Y.-S. Guan, Y. Hu, Y. Huang, A. F. Cannella, C. Li, J. N. Armstrong and S. Ren, ACS Appl. Nano Mater., 2019, 2, 1140-1145.
8   D. Jérome, Organic Conductors: Chem. Rev. 2004, 104, 5565-5592.
9   Y. Kobayashi, T. Terauchi, S. Sumi, Y. Matsushita, Nat. Mater. 2017, 16, 109-114.
10 H. Alves, A. S. Molinari, H. Xie, A. F. Morpurgo, Nat. Mater. 2008, 7, 574-580.
11 L. Zuppiroli, S. Bouffard, K. Bechgaard, B. Hilti, C. W. Mayer, Phys. Rev. B 1980, 22, 6035-6043.
12 T. Kawamoto, K. Kurata, T. Mori, R. Kumai, Magnetochemistry 2017, 3, 14.
13 S. Jeon, P. W. Doak, B. G. Sumpter, P. Ganesh, P. Maksymovych, ACS Nano 2016, 10, 7821-7829.
14 J. Fraxedas, S. Molas, A. Figueras, I. Jiménez, R. Gago, P. Auban-Senzier, M. Goffman, J. Solid State Chem. 2002, 168, 384-389.
15 K. Shibata, H. Wada, K. Ishikawa, H. Takezoe, T. Mori, Appl. Phys. Lett. 2007, 90, 193509.
16 C. W. Chu, J. M. E. Harper, T. H. Geballe, R. L. Greene, Phys. Rew. Lett. 1973, 31, 1491-1494.
17 V. Solovyeva, A. Cmyrev, R. Sachser, H. Reith, M. Huth, J. Phys. D: Appl. Phys. 2011, 44, 385301.
18 M. J. Cohen, L. B. Coleman, A. F. Garito, A. J. Heeger, Phys. Rev. B 1974, 10, 1298-1307.
19 M. Sakai, M. Iizuka, M. Nakamura, K. Kudo, Synth. Met. 2005, 153, 293-296.
20 S. Haas, Y. Takahashi, K. Takimiya, T. Hasegawa, Appl. Phys. Lett. 2009, 95, 022111.
21 M. Sakai, M. Nakamura, K. Kudo, Appl. Phys. Lett. 2007, 90, 062101.
22 Y. Takahashi, T. Hasegawa, Y. Abe, Y. Tokura, G. Saito, Appl. Phys. Lett. 2006, 88, 073504.
23 Goudappagouda, S. Chithiravel, K. Krishnamoorthy, S. W. Gosavi, S. Santhosh Babu, Chem. Commun. 2015, 51, 10439-10442.
24 R. H. Friend, M. Miljak, D. Jérome, Phys. Rew. Lett. 1978, 40, 1048-1051.
25 C. Weyl, D. Jérome, P. M. Chaikin, K. Bechgaard, J. Physique 1982, 43, 1167-1172.
26 Y. Singh, Advances in Materials Physics and Chemistry 2017, 07, 375-394.
27 K. Murata, K. Yokogawa, S. Arumugam, H. Yoshino, Crystals 2012, 2, 1460-1482.
28 M. Vosgueritchian, D. J. Lipomi, Z. Bao, Adv. Funct. Mater. 2012, 22, 421-428.
29 Y. H. Kim, C. Sachse, M. L. Machala, C. May, L. Müller-Meskamp, K. Leo, Adv. Funct. Mater. 2011, 21, 1076-1081.
30 Y. Hanyu, I. Honma, Sci Rep. 2012, 2, 453.
31 H. J. Yen, H. Tsai, M. Zhou, E. F. Holby, S. Choudhury, A. Chen, L. Adamska, S. Tretiak, T. Sanchez, S. Iyer, Adv. Mater. 2016, 28, 10250-10256.